Grading of gliomas using 3D CEST imaging with compressed sensing and sensitivity encoding

和田, 達弘

European Journal of Radiology 158 (2023) 110654

Contents lists available at ScienceDirect

European Journal of Radiology

journal homepage: www.elsevier.com/locate/ejrad

Grading of gliomas using 3D CEST imaging with compressed sensing and sensitivity encoding

Tatsuhiro Wada [a,b,*], Osamu Togao [c], Chiaki Tokunaga [a], Masahiro Oga [a], Kazufumi Kikuchi [d], Koji Yamashita [d], Hidetaka Yamamoto [e], Masami Yoneyama [f], Koji Kobayashi [a], Toyoyuki Kato [a], Kousei Ishigami [d], Hidetake Yabuuchi [g]

[a] Division of Radiology, Department of Medical Technology, Kyushu University Hospital, Japan
[b] Department of Health Sciences, Graduate School of Medical Sciences, Kyushu University, Japan
[c] Department of Molecular Imaging & Diagnosis, Graduate School of Medical Sciences, Kyushu University, Japan
[d] Department of Clinical Radiology, Graduate School of Medical Sciences, Kyushu University, Japan
[e] Department of Anatomic Pathology, Pathological Sciences, Graduate School of Medical Sciences, Kyushu University, Japan
[f] Philips Japan, Japan
[g] Department of Health Sciences, Faculty of Medical Sciences, Kyushu University, Japan

ARTICLE INFO

Keywords:
Glioma
Chemical exchange saturation transfer
Compressed sensing and sensitivity encoding
Multi-slice chemical exchange saturation transfer imaging

ABSTRACT

Purpose: We evaluated the usefulness of three-dimensional (3D) chemical exchange saturation transfer (CEST) imaging with compressed sensing and sensitivity encoding (CS-SENSE) for differentiating low-grade gliomas (LGGs) from high-grade gliomas (HGGs).

Methods: We evaluated 28 patients (mean age 51.0 ± 13.9 years, 13 males, 15 females) including 12 with LGGs and 16 with HGGs, all acquired using a 3 T magnetic resonance (MR) scanner. Nine slices were acquired for 3D CEST imaging, and one slice was acquired for two-dimensional (2D) CEST imaging. Two radiological technologists each drew a region of interest (ROI) surrounding the high-signal-intensity area(s) on the fluid-attenuated inversion recovery image of each patient. We compared the magnetization transfer ratio asymmetry (MTRasym) at 3.5 ppm in the tumors among the (*i*) single-slice 2D CEST imaging ("2D"), (*ii*) all tumor slices of the 3D CEST imaging ($3D_{all}$), and (*iii*) a representative tumor slice of 3D CEST imaging (maximum signal intensity [$3D_{max}$]). The relationship between the MTRasym at 3.5 ppm values measured by these three methods and the Ki-67 labeling index (LI) of the tumors was assessed. Diagnostic performance was evaluated with a receiver operating characteristic analysis. The Ki-67LI and MTRasym at 3.5 ppm values were compared between the LGGs and HGGs.

Results: A moderate positive correlation between the MTRasym at 3.5 ppm and the Ki-67LI was observed with all three methods. All methods proved a significantly larger MTRasym at 3.5 ppm for the HGGs compared to the LGGs. All methods showed equivalent diagnostic performance. The signal intensity varied depending on the slice position in each case.

Conclusions: The 3D CEST imaging provided the MTRasym at 3.5 ppm for each slice cross-section; its diagnostic performance was also equivalent to that of 2D CEST imaging.

1. Introduction

Chemical exchange saturation transfer (CEST) is a magnetic resonance imaging (MRI) technique that provides image contrast and reflects various metabolites in vivo [1]. Amide proton transfer (APT)-weighted imaging is a type of endogenous CEST imaging that reflects amide protons (−NH) with a resonance frequency at +3.5 ppm from bulk water [2,3]. The contrast of APT-weighted imaging depends on the concentration of mobile protein peptides, the pH, and the temperature in vivo. APT-weighted imaging has been reported to be useful for predicting the histological grades of gliomas [3–5], for differentiating recurrent glioma tumors and radiation necrosis [6,7], and for detecting pH change lesion in acute stroke [8,9].

Differentiating low-grade glioma (LGG) and high-grade glioma

* Corresponding author at: Division of Radiology, Department of Medical Technology, Kyushu University Hospital, Japan.
E-mail address: wada.tatsuhiro.285@m.kyushu-u.ac.jp (T. Wada).

https://doi.org/10.1016/j.ejrad.2022.110654
Received 5 October 2022; Received in revised form 2 December 2022; Accepted 12 December 2022
Available online 15 December 2022

Table 1
Patient characteristics.

Group	Patient	Age	Sex	WHO grade	Histology	Ki-67 (%)
LGG	1	59	F	2	Astrocytoma, IDH-mutant	5
	2	47	F	2	Astrocytoma, IDH-mutant	5
	3	36	M	2	Astrocytoma, IDH-mutant	5
	4	35	M	2	Astrocytoma, IDH-mutant	5
	5	50	F	2	Astrocytoma, IDH-mutant	5
	6	44	F	2	Astrocytoma, IDH-mutant	7
	7	42	F	2	Astrocytoma, IDH-mutant	8
	8	31	F	2	Astrocytoma, IDH-mutant	10
	9	55	M	2	Oligodendroglioma, IDH-mutant & 1p19q codeleted	2
	10	47	M	2	Oligodendroglioma, IDH-mutant & 1p19q codeleted	4
	11	41	M	2	Oligodendroglioma, IDH-mutant & 1p19q codeleted	5
	12	40	F	2	Oligodendroglioma, IDH-mutant & 1p19q codeleted	5
HGG	13	50	F	3	Astrocytoma, IDH-mutant	8
	14	60	F	3	Astrocytoma, IDH-mutant	10
	15	38	M	3	Astrocytoma, IDH-mutant	10
	16	27	F	3	Astrocytoma, IDH-wildtype	8
	17	33	F	3	Astrocytoma, IDH-wildtype	10
	18	70	M	3	Astrocytoma, IDH-wildtype	20
	19	65	M	3	Oligodendroglioma, IDH-mutant & 1p19q codeleted	15
	20	68	M	3	Oligodendroglioma, IDH-mutant & 1p19q codeleted	30
	21	72	F	3	Oligodendroglioma, IDH-mutant & 1p19q codeleted	40
	22	47	F	4	Glioblastoma, IDH-wildtype	10
	23	62	F	4	Glioblastoma, IDH-wildtype	10
	24	68	M	4	Glioblastoma, IDH-wildtype	30
	25	54	M	4	Glioblastoma, IDH-wildtype	40
	26	44	M	4	Glioblastoma, IDH-wildtype	40
	27	61	F	4	Glioblastoma, IDH-wildtype	60
	28	83	M	4	Glioblastoma, IDH-wildtype	70

HGG: high-grade glioma, LGG: low-grade glioma.

(HGG) with the use of single-slice two-dimensional (2D) CEST imaging has been described [3–5]. LGGs have been shown to be mostly isointense on APT-weighted imaging, whereas HGGs showed increased signal intensity on APT-weighted imaging. An advantage of CEST imaging is that it can be quantitatively evaluated using the signal values of APT-weighted imaging [4]. However, considering the heterogeneity within tumors [10–12], the signal values of APT-weighted imaging may differ depending on the imaging cross-section. CEST imaging in multiple cross-sections is thus desirable. Multi-slice APT-weighted imaging techniques using 2D imaging have been proposed [13,14], but the signal loss of multi-slice imaging is a T1 relaxation loss due to the imaging order of the slices. Compared to multi-slice imaging, 3D imaging is more suitable for volume APT-weighted imaging because it has less inter-slice relaxation loss, wider volume coverage, a higher signal-to-noise ratio, and a shorter acquisition time[15].

A compressed sensing (CS) and sensitivity encoding (SENSE) technique (CS-SENSE) has been proposed to accelerate the MR acquisition time [16]. The CS-SENSE acceleration technique applies randomized non-uniform variable density k-space subsampling, which is designed to promote incoherence, instead of the regular under-sampling applied in conventional SENSE. It was reported that accelerated CEST imaging combined with parallel imaging and CS had the highest accuracy in CEST reconstruction compared to accelerated CEST imaging using only parallel imaging or CS [17]. We demonstrated that 3D CEST imaging with CS-SENSE might be able to obtain the same contrast as that provided by 2D CEST imaging with full data sampling (without an acceleration method; e.g., SENSE) in brain tumors at 3T [18].

We conducted the present study to evaluate the usefulness of 3D CEST imaging with CS-SENSE for differentiating LGGs from HGGs. We compared MTRasym at 3.5 ppm of the tumors among (*i*) single-slice 2D CEST imaging, (*ii*) all tumor slices of 3D CEST imaging, and (*iii*) a representative tumor slice of 3D CEST imaging (maximum signal values).

2. Materials and methods

2.1. Patients

Twenty-eight consecutive patients with a postoperative diagnosis of glioma between July 2020 and November 2021 were included. Exclusion criterion was severe image artifacts caused by patient's motion. Four cases were excluded for this reason. We analyzed the cases of 28 patients with glioma (mean age 51.0 ± 13.9 years, 13 males and 15 females) who underwent a subsequent surgical resection. Twelve patients with LGGs (World Health Organization [WHO] grade 2), and 16 patients with HGGs (WHO grade 3 or 4) were identified. The characteristics of patients are summarized in Table 1. The histological diagnosis was determined based on WHO classification of central nervous system (CNS) tumors 5th edition [19]. This study was approved by the Our Institutional Review Board, and the patients' informed consent for their images to be used was obtained.

2.2. Pathological evaluation

The pathological diagnosis was determined with specimens removed at surgical resection according to the 2021 WHO classification of CNS tumors by established neuropathologist (H.Y., 22 years of experience). In addition to the conventional histopathological evaluation, the Ki-67 labeling index (LI) was determined using the standard procedure. Briefly, fields with the highest number of Ki-67 – labeled cells were initially selected through a generalized survey, and then the percentage of positively labeled cells was determined by counting more than 1000 tumor nuclei at × 200 magnification. The isocitrate dehydrogenase (IDH) mutation and 1p19q-codelation status was confirmed in all patients by the methods described [19]. All histopathological findings of this study are described in Table 1.

2.3. MR imaging protocol

For all of the patients, MR imaging was performed on a 3-T clinical MR scanner (Ingenia 3.0 T, Philips Healthcare, Best, The Netherlands) using a 20-channel head-neck coil. The 2D CEST sequences were acquired with 32 frequency offsets (±16, ±12, ±8, ±6, ±5.5, ±5, ±4.5, ±4, ±3.5, ±3, ±2.5, ±2, ±1.5, ±1, ±0.5, 0, and −1560 ppm) using the single-shot turbo-spin echo (TSE) sequence with driven equilibrium refocusing and the following parameters: radiofrequency (RF) saturation with 2.0 sec duration and 2.0 μT power, field of view (FOV) = 230 × 230 mm^2, matrix = 128 × 128 (reconstructed to 256 × 256), voxel size = 1.8 × 1.8 × 5 mm^3, TR/TE = 6642/5.3 msec, echo train length (ETL) = 128, no parallel imaging, and the scan time = 3 min 39 sec for a single slice. The 2D B0 map was obtained separately using a 2D gradient-echo (GRE) sequence with the following parameters: FOV = 230 × 230 mm^2, matrix = 128 × 128 (reconstructed to 256 × 256), voxel size = 1.8 × 1.8 × 5 mm^3, TR/TE = 16/8.2 msec; flip angle = 30°, dual echo (Δ TE = 1 msec), number of acquisitions = 8, and scan time = 32 sec.

The 3D CEST sequences were acquired with 26 frequency offsets (±6, ±5.5, ±5, ±4.5, ±4, ±3.5, ±3, ±2.5, ±2, ±1.5, ±1, ±0.5, 0, and

Table 2
Size of the ROIs in 2D and 3D CEST imaging by each observer and the ICC between the two observers.

CEST imaging	ROI size*, cm^2: average ± SD (min. – max.)		ICC
	Observer 1	Observer 2	
2D	33.18 ± 25.27 (7.32–117.83)	37.89 ± 28.84 (7.65–146.25)	0.93
3D	29.01 ± 22.85 (2.49–117.83)	32.60 ± 24.94 (2.46–132.81)	0.96

*One pixel = 0.0324 cm^2. ICC: intra-class correlation coefficient, max: maximum size of region of interest (ROI), min: minimum size of ROI, SD: standard deviation.

−1560 ppm) using the multi-shot TSE sequence with driven equilibrium refocusing and the following parameters: RF saturation with 2.0 sec duration and 2.0 μT power, nine slices, FOV = 230 × 201 × 45 mm^3, matrix = 128 × 112 (reconstructed to 256 × 256), voxel size = 1.8 × 1.8 × 5 mm^3, TR/TE = 5586/5.9 msec, ETL = 122, CS-SENSE factor = 4, and scan time = 5 min 1 sec for nine slices. A 3D B0 map was obtained separately using a 3D GRE sequence with the following parameters: nine slices, FOV = 230 × 201 × 45 mm^3, matrix = 128 × 112 (reconstructed to 256 × 256), voxel size = 1.8 × 1.8 × 5 mm^3, TR/TE = 14/7.5 msec; flip angle = 35°, dual-echo (Δ TE = 1 msec), CS-SENSE factor = 2, number of acquisitions = 1, and scan time = 45 sec. The imaging section center of the 3D CEST imaging was set to the imaging section of the 2D CEST imaging.

To cover the entire brain, fluid-attenuated inversion recovery (FLAIR) images were acquired in sagittal sections, using the following parameters: FLAIR (3D FLAIR, TR/TE = 4000/245 msec, inversion time = 1600 msec, matrix = 288 × 288, and voxel size = 0.87 × 0.87 × 1.40 mm^3.

2.4. Image analysis

All image data were analyzed using the software program ImageJ (ver. 1.52a; U.S. National Institutes of Health, Bethesda, MD). A dedicated plug-in was created to assess the magnetization transfer ratio

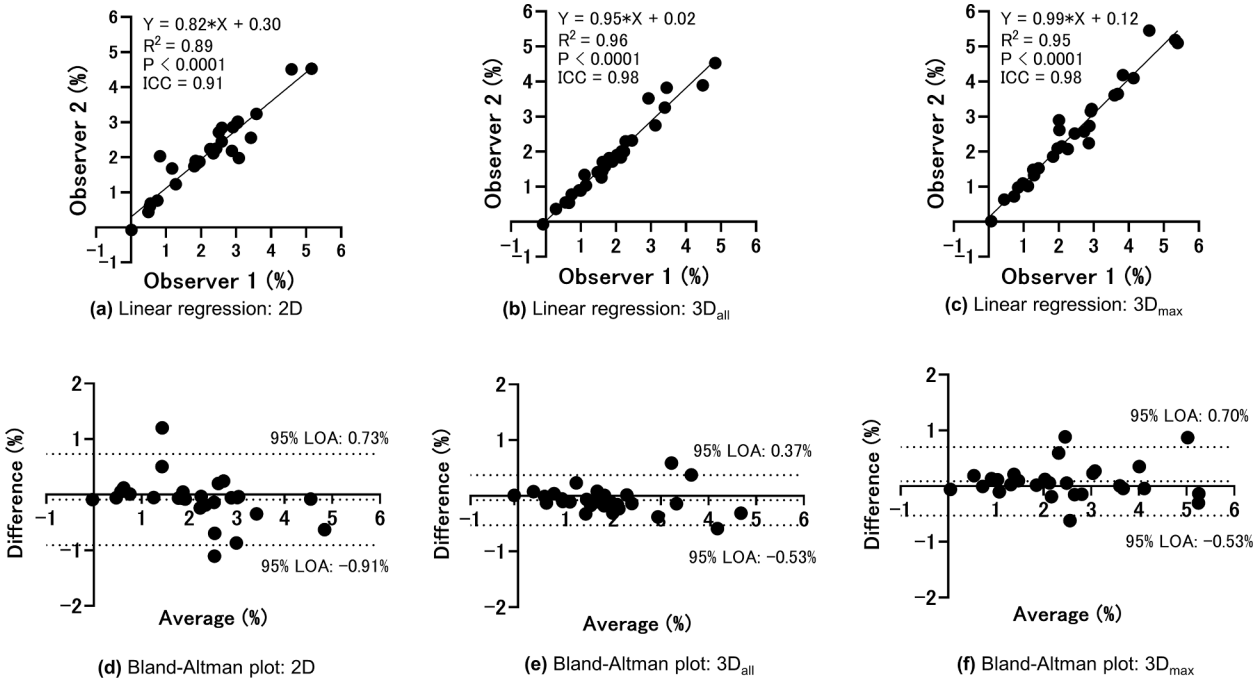

Fig. 1. Analyses of interobserver agreement. The linear regression analyses the MTRasym at 3.5 ppm measured by the two observers shows high correlation for the **(a)** 2D, **(b)** $3D_{all}$, and **(c)** $3D_{max}$ methods. The Bland-Altman analyses of the MTRasym at 3.5 ppm measured by the two observers shows high concordance for the **(d)** 2D, **(e)** $3D_{all}$, and **(f)** $3D_{max}$ methods.

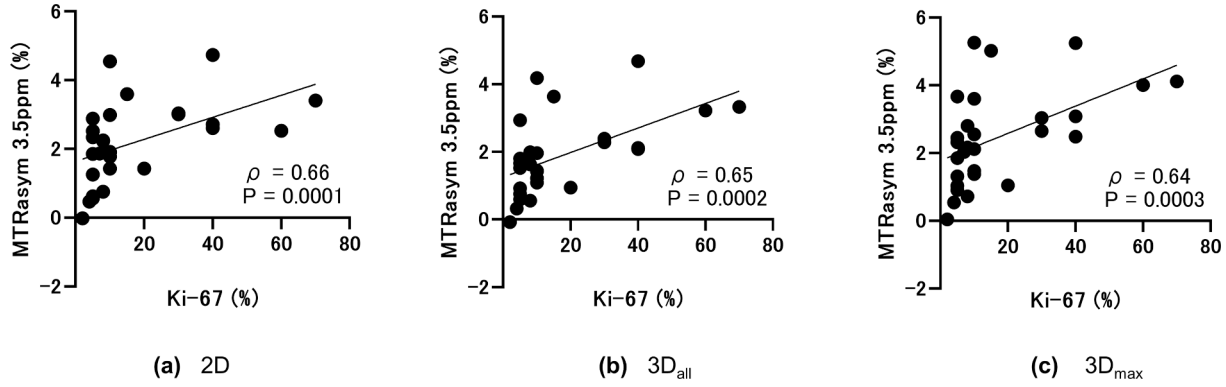

Fig. 2. Correlation between the MTRasym at 3.5 ppm and the Ki-67LI for the **(a)** 2D, **(b)** $3D_{all}$, and **(c)** $3D_{max}$ methods. Moderate positive correlations were observed with each method.

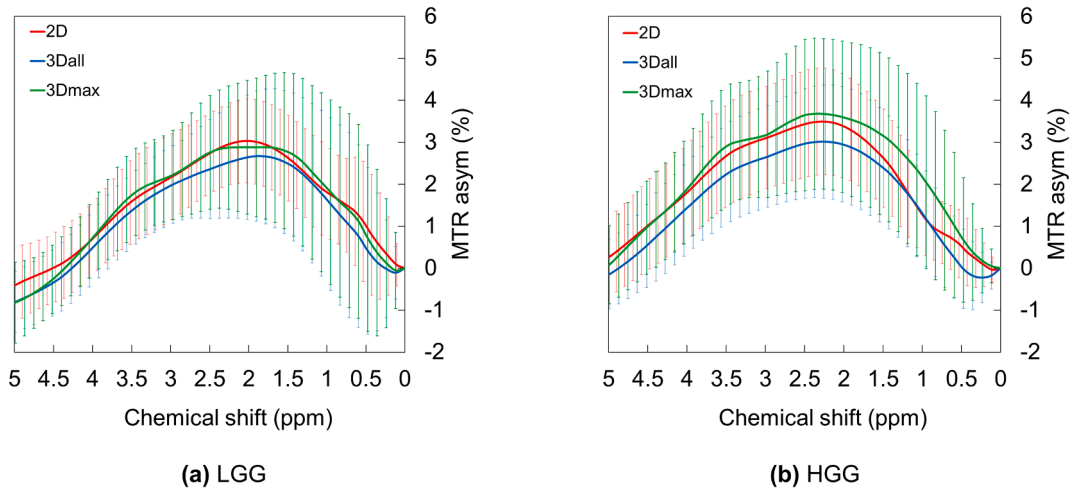

Fig. 3. Comparison of the MTRasym at 3.5 ppm spectra of 2D, $3D_{all}$, and $3D_{max}$ for the low-grade gliomas (LGGs) **(a)** and high-grade gliomas (HGGs) **(b)**. The CEST effects of both the LGGs and HGGs were observed in the frequency offset range from 1.5 ppm to 4.0 ppm for all three methods.

Table 3
The Ki-67 labeling index and MTRasym 3.5 ppm in the LGGs and HGGs.

Parameter	LGG	HGG	p-value
Ki-67LI, %	5.50 ± 2.02	23.94 ± 21.48	<0.0001
MTRasym 3.5 ppm, %			
2D	1.54 ± 0.94	2.67 ± 1.09	0.0083
$3D_{all}$	1.28 ± 0.81	2.32 ± 1.20	0.0130
$3D_{max}$	1.74 ± 1.01	3.00 ± 1.46	0.0150

HGG: high-grade glioma, LGG: low-grade glioma, LI: labeling index, MTRasym: magnetization transfer ratio asymmetry, $3D_{all}$: all ROIs in 3D CEST imaging, $3D_{max}$: the slice with the max. mean value of the MTRasym at 3.5 ppm.

asymmetry (MTRasym) and was equipped with a correction function for B0 inhomogeneity. To reduce undesirable affects from conventional MT effects and direct water saturation, the MTRasym with respects to bulk water frequency was performed. The MTRasym was defined as:

$$MTR_{asym}(\Delta ppm) = \frac{S_{sat}(-\Delta ppm) - S_{sat}(+\Delta ppm)}{S_0}$$

where $S_{sat}(\Delta ppm)$ and S_0 are the signal intensities at a target frequency and −1560 ppm, respectively.

Regions of interest (ROIs) were drawn on the raw 2D or 3D GRE image to calculate the 2D or 3D B0 map with reference to the FLAIR image. The high signal intensity areas on the FLAIR image were surrounded. The ROIs were copied onto each MTRasym image. ROIs were manually drawn by the two radiology technologists (T.W., 17 years of experience and M.O., 19 years of experience) to include the entire tumor region. We defined MTRasym at 3.5 ppm in the tumors among the (*i*) single-slice 2D CEST imaging ("2D"), (*ii*) all tumor slices of the 3D CEST imaging ($3D_{all}$), and (*iii*) a representative tumor slice of 3D CEST imaging (maximum signal intensity [$3D_{max}$]).

2.5. Statistical analyses

The intra-class correlation coefficient (ICC) was calculated to evaluate the interobserver agreement regarding the sizes of the ROIs created by the two readers. For the assessment of the interobserver agreement concerning the tumor MTRasym at 3.5 ppm values obtained by the two readers, the ICC was calculated; a simple linear regression analysis was performed. A Bland-Altman plot analysis was also conducted. Since the MTR_{sym} at 3.5 ppm values measured by the two observers agreed well, we averaged these values for each patient in the analyses. Spearman's rank correlations were calculated for a determination of the statistical correlation between the mean value of MTRasym at 3.5 ppm in all three methods and the Ki-67LI. The Ki-67LI and mean values of MTRasym at

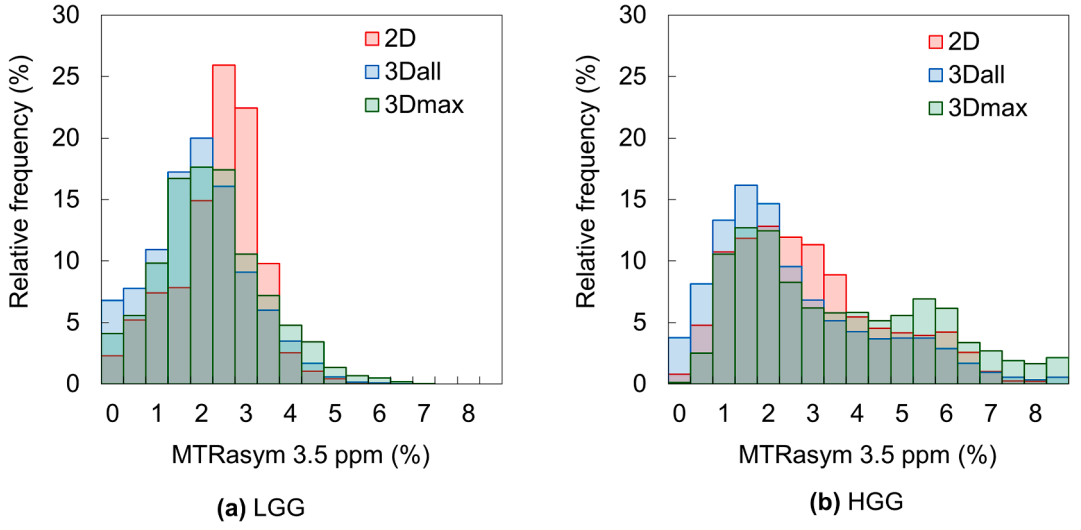

Fig. 4. Histograms of MTRasym at 3.5 ppm for all methods in the LGG and HGG groups. The distribution of the MTRasym values at 3.5 ppm was concentrated around 2–3 (%) in the LGG group. In the HGG group, the MTRasym at 3.5 ppm of the $3D_{max}$ method was observed >5% more often than with the other two methods.

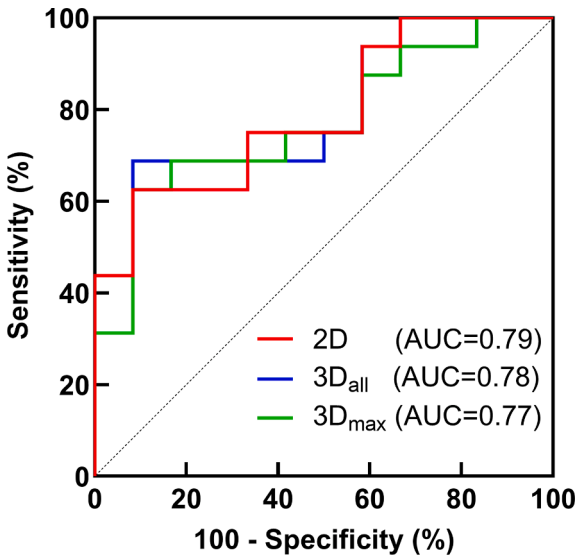

Fig. 5. Receiver operating characteristic curve analyses for the differentiation of LGGs from HGGs. All three imaging methods showed medium diagnostic performance.

Table 4
Receiver operating characteristic curve analysis for the differentiation of LGGs and HGGs.

Method	AUC	Cutoff value (%)	Sensitivity (%)	Specificity (%)
2D	0.79	2.52	91.7	62.5
$3D_{all}$	0.78	1.81	91.7	68.8
$3D_{max}$	0.77	2.55	91.7	62.5

AUC: area under the receiver operating characteristic curve.

3.5 ppm in all three methods were compared between the LGG and HGG groups by the Mann-Whitney *U* test. Receiver operating characteristic (ROC) and area under the curve (AUC) analyses were performed to evaluate the diagnostic performance of the parameters for differentiating LGGs from HGGs. The statistical analyses were performed with GraphPad Prism 9 and JMP pro 16.0 software. P-values < 0.05 were considered significant in all analyses.

3. Results

The interobserver agreement between the two observers regarding the ROI size was excellent for both the 2D CEST imaging (0.93) and the 3D CEST imaging (0.96) (Table 2). The two readers' interobserver agreement for the MTRasym at 3.5 ppm of the 28 patients' tumors was also excellent, with the ICC of 0.91–0.98 and the R^2 of 0.89–0.96 (Fig. 1a–c). The Bland-Altman plots showed that the MTRasym at 3.5 ppm measured with 2D CEST imaging (Fig. 1d) resulted in a small bias of −0.09% and narrow 95% limits of agreement (from −0.91% to 0.73%). The MTRasym at 3.5 ppm values measured as $3D_{all}$ (Fig. 1e) showed a similar bias of −0.08% and narrower 95% limits of agreement (from −0.53% to 0.37%) compared to the values measured with 2D. The MTRasym at 3.5 ppm values measured as the $3D_{max}$ (Fig. 1f) showed a similar bias of −0.09% and slightly narrower 95% limits of agreement (from −0.53% to 0.70%) compared to those measured with 2D.

Fig. 2 illustrates the relationship between the MTRasym at 3.5 ppm and Ki-67LI for all three methods, i.e., (*i*) single-slice 2D CEST imaging (2D), (*ii*) all tumor slices of 3D CEST imaging ($3D_{all}$), and (*iii*) a representative tumor slice of 3D CEST imaging (max. signal values; $3D_{max}$). A moderate positive correlation between the MTRasym at 3.5 ppm and the Ki-67LI was observed with the 2D ($\rho = 0.66$, $p = 0.0001$), $3D_{all}$ ($\rho = 0.65$, $p = 0.0002$), and $3D_{max}$ ($\rho = 0.64$, $p = 0.0003$) methods.

The MTRasym spectra of LGG and HGG for each method are given in Fig. 3. The maximum peak of the MTRasym spectra in the LGGs and HGGs for all methods were observed at around 2.0 ppm and at 2.5 ppm, respectively. The MTRasym spectra of the HGGs were gradually decreased with a maximum peak at 2.5 ppm in 2D and in $3D_{all}$, but another peak was observed at 3.5 ppm in $3D_{max}$.

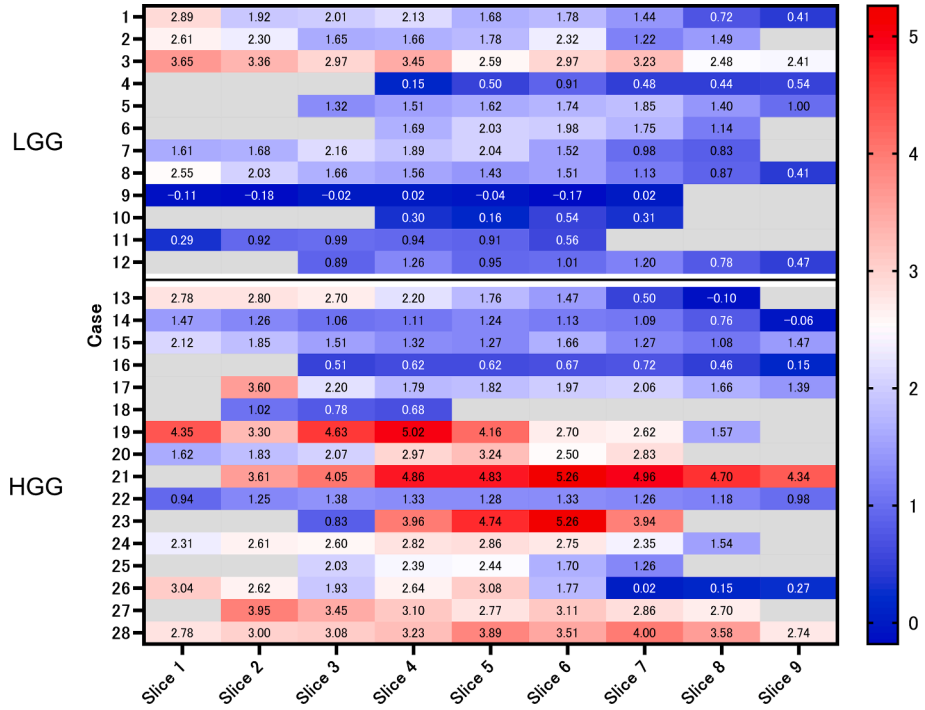

Fig. 6. Heatmap showing the mean value of MTRasym at 3.5 ppm in each slice for each patient's case. The signal intensity varied depending on the slice position in each case.

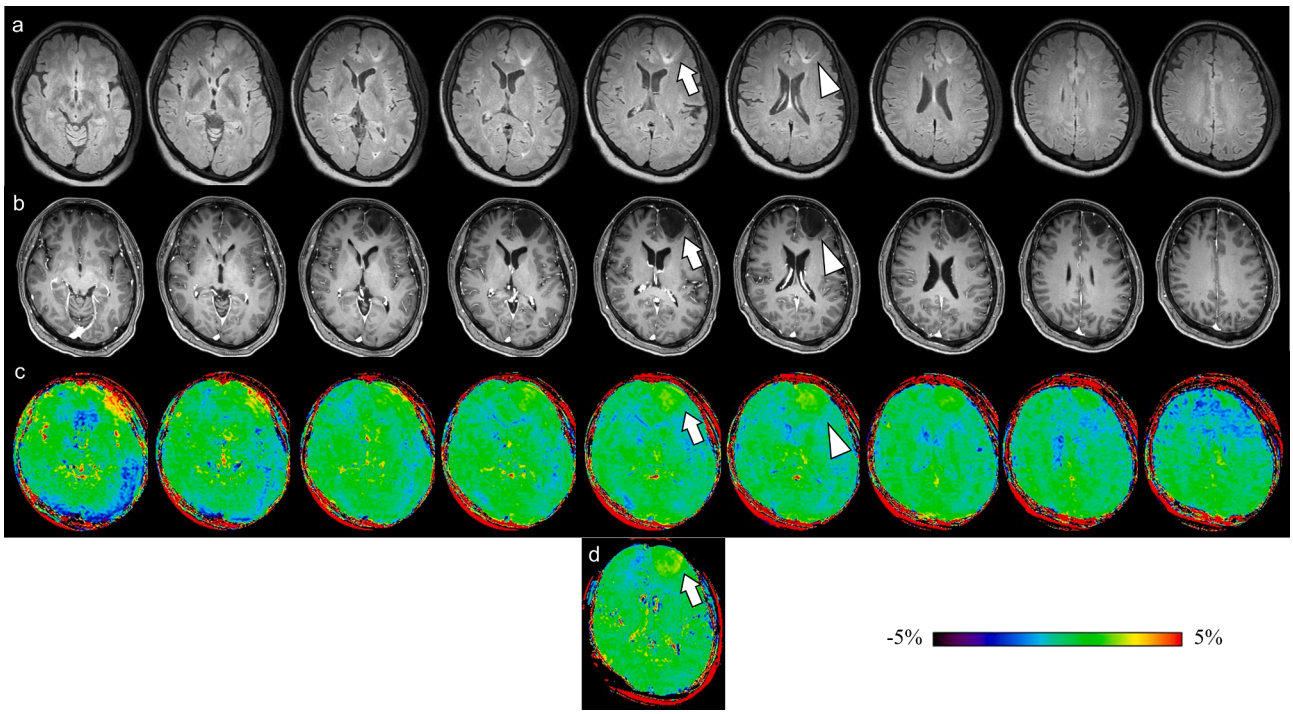

Fig. 7. Astrocytoma, IDH-mutant, CNS WHO grade 2 in a 50-year-old female. **(a)** FLAIR, **(b)** Gd T1WI, **(c)** 3D MTRasym at 3.5 ppm, and **(d)** 2D MTRasym at 3.5 ppm. The MTRasym values at 3.5 ppm for the 2D (*arrow*), $3D_{all}$, and $3D_{max}$ (*arrowhead*) methods were 1.85 ± 0.49, 1.55 ± 1.10, and 1.85 ± 0.82, respectively. Both the 2D MTRasym at 3.5 ppm (d) and the 3D MTRasym at 3.5 ppm (c) showed a mild increase in the signal intensity in lesions with high signal intensity on FLAIR imaging (a). Similar signal intensities in multi-slices of the 3D MTRasym at 3.5 ppm (c) were observed in high-signal legions on the FLAIR images (a).

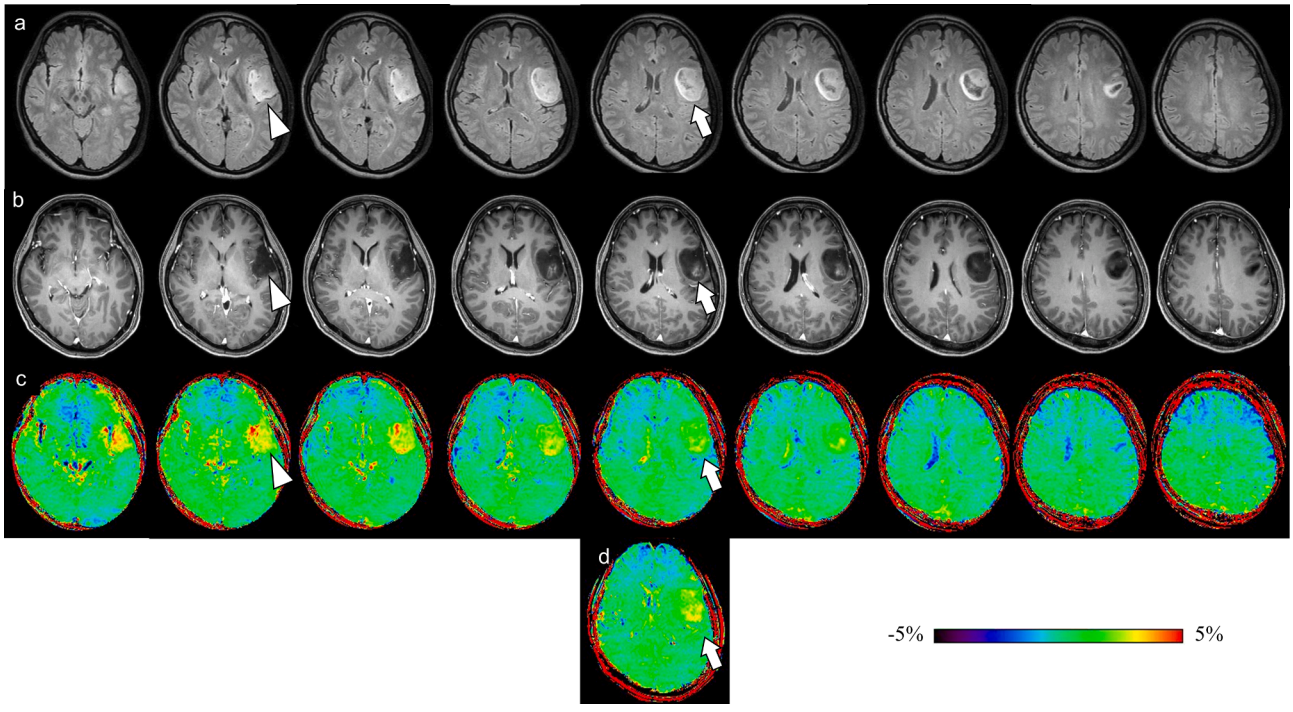

Fig. 8. Astrocytoma, IDH-mutant, CNS WHO grade 3 in a 50-year-old female. **(a)** FLAIR, **(b)** Gd T1WI, **(c)** 3D MTRasym at 3.5 ppm, and **(d)** 2D MTRasym at 3.5 ppm. The MTRasym at 3.5 ppm for the 2D (*arrow*), $3D_{all}$, and $3D_{max}$ (*arrowhead*) methods were 2.20 ± 0.60, 2.00 ± 1.06, and 2.80 ± 0.80, respectively. Both the 2D MTRasym at 3.5 ppm and the 3D MTRasym at 3.5 ppm showed a mild increase in signal intensity in the lesion with contrast enhancement (*arrows* in b–d). However, the signal intensity varied depending on the slice position, and the 2D MTRasym at 3.5 ppm image (d) was not the same slice position as that for the $3D_{max}$ (c, *arrowhead*).

Table 3 lists the measurements in the LGG and HGG groups. The Ki-67LI was significantly larger in the HGG group compared to the LGG group, and the mean value of MTRasym at 3.5 ppm was significantly larger in the HGG group compared to the LGG group in all three methods. Fig. 4 provides the histogram profiles for all methods. The distribution of the MTRasym at 3.5 ppm for the LGG group in the 2D was concentrated at around 2–3 (%), and the MTRasym at 3.5 ppm obtained by both the $3D_{all}$ and $3D_{max}$ methods were lower than in the 2D method. In the HGG group, the higher MTRasym at 3.5 ppm shown by the $3D_{max}$ method was observed than in the other methods.

Fig. 5 and Table 4 concern the diagnostic performance of the methods as determined by the ROC analyses for differentiating LGGs from HGGs. Equivalent AUCs were obtained in all three methods. The specificities were the same for all methods, but the sensitivity of the 2D was lower than that of both the $3D_{all}$ and $3D_{max}$.

The MTRasym at 3.5 ppm values measured within the ROI on each slice for each patient are depicted in Fig. 6. The signal intensity varied depending on the slice position in each case.

Figs. 7 and 8 are images from a representative case of astrocytoma, IDH-mutant, CNS WHO grade 2 and astrocytoma, IDH-mutant, CNS WHO grade 3, respectively. Similar signal intensities by both 2D MTRasym at 3.5 ppm (Fig. 7d, Fig. 8d, arrows) and the same slice position of 3D MTRasym at 3.5 ppm (Fig. 7c, 8c, arrows) were observed in each case. Notably, the signal intensity varied depending on the slice position in the grade 3 astrocytoma (Fig. 8c). The image from the 2D MTRasym at 3.5 ppm (Fig. 8d) was not the same slice position for the $3D_{max}$ in the grade 3 tumor (Fig. 8c, arrowhead).

4. Discussion

The results of our analyses demonstrated the usefulness of 3D CEST imaging with CS-SENSE in glioma grading. The evaluation of the entire tumors by multi-slice CEST imaging was important in the gliomas' grading because the signal intensities differed among the tumor slices.

CEST imaging can detect various compounds in vivo. The MTRasym in both LGGs and HGGs has been reported to have a broad peak ranging from 1.5 ppm to 4.0 ppm [2,20]. We were able to detect peaks from 1.5 ppm to 4.0 ppm in the present study by using 3D CEST imaging with CS-SENSE. The grading of gliomas using CEST imaging at 3 T is often reported for APT-weighted imaging using a MTRasym at 3.5 ppm, which reflects amide protons. It has been reported that the signal intensity of APT-weighted imaging is positively correlated with the Ki-67 labeling index [4], which is a pathological marker of cell proliferation; this suggested that APT-weighted imaging reflects tumor cell activity. The correlation between MTRasym at 3.5 ppm and the Ki-67 labeling index in the present 3D CEST imaging with CS-SENSE was comparable to that of the APT-weighted imaging in previous studies. The multi-slice 3D CEST imaging was able to reflect tumor cell activity.

Our analyses also revealed that the AUCs of both the $3D_{all}$ and $3D_{max}$ methods were similar to those of conventional 2D CEST imaging. A 3D CEST imaging protocol with CS-SENSE can thus be used for glioma grading, like 2D CEST imaging. We observed an increase in lower signal intensities in MTRasym at 3.5 ppm for both $3D_{all}$ and $3D_{max}$ compared to 2D CEST imaging. In a study of in non-enhancing gliomas, Warnet et al. used 3D CEST imaging to detect amide protons by conducting a Lorentzian fit analysis (LDamide), and they reported that not all slices of the tumors in each imaging section necessarily showed high signal intensity for LDamide [21]. In the present study, the low-signal intensities of MTRasym at 3.5 ppm in the 3D CEST imaging increased because the high-signal area in the FLAIR image reflecting edema was included in the region of interest setting for the 3D CEST imaging.

The advantage of 3D CEST imaging is that multi-slice CEST images can be used for glioma grading. Sakata et al. reported that a glioma grade diagnosis can be made using only representative slices with reference to multi-slice FLAIR images, and they described the possibility of reduced imaging time by acquiring a representative 2D CEST image rather than acquiring 3D CEST images [22]. On the other hand, the same acquisition time as that necessary for 2D CEST imaging might be achievable with 3D CEST imaging with CS-SENSE. It is therefore possible to determine a representative single-slice cross-section from 3D CEST imaging with reference to both multi-slice FLAIR images.

The use of 3D CEST imaging with the GRE sequence has been reported in several investigations [23–25], as the TSE sequence needs a longer acquisition time than the GRE sequence. However, Doneva et al. reported that the 3D TSE CEST sequence has the advantage of a higher signal-to-noise ratio and signal uniformity compared to the 3D gradient and spin echo sequence [23]. The TSE-based 3D CEST imaging used in the present study was combined with CS-SENSE to reduce the acquisition time (5 min 1 sec), which is essentially the same acquisition time as those for 3D APT-weighted imaging with the GRE sequence (5 min 31 sec) [22] and TSE sequence (4 min 30 sec) [26]. Thus, 3D CEST imaging with CS-SENSE is as clinically applicable as 3D APT-weighted imaging.

There are several limitations to this study. The number of patients was small (~11 for both the LGGs and the HGGs). Many imaging sequences for preoperative examinations are performed other than CEST imaging, and not all of them can be obtained in all cases. Further analyses based on larger numbers of patients are desirable. Second, CEST imaging does not take each component into account because it includes various factors such as direct water saturation, the nuclear Overhauser effect, MT effects, and more. It is desirable to detect each component by a multi-pool analysis and Lorentzian fitting [27]. However, in order to detect the components, it is necessary to use a weaker pulse (e.g., 0.6 μT) than the saturation pulse strength (2 μT) used in this study. The imaging parameters that we used made it difficult to detect individual components. In addition, since a high magnetic field is ideal, future applications are expected.

5. Conclusion

We investigated the usefulness of 3D CEST imaging with CS-SENSE for glioma grading, including the entire tumor. The signal intensity of gliomas varies in each imaging section was demonstrated by using multi-slice 3D CEST imaging with CS-SENSE. Both the diagnostic performance of $3D_{all}$ and $3D_{max}$ using 3D CEST imaging were equivalent to that of 2D CEST imaging. 3D CEST imaging with CS-SENSE can be used clinically for glioma grading as well as 2D CEST imaging.

Declaration of Competing Interest

The authors declare that they have no known competing financial interests or personal relationships that could have appeared to influence the work reported in this paper.

Acknowledgments

This work was supported by a grant from the Japan Society for the Promotion of Science (JSPS) KAKENHI, no. JP19K17145.

References

[1] K.M. Ward, A.H. Aletras, R.S. Balaban, A new class of contrast agents for MRI based on proton chemical exchange dependent saturation transfer (CEST), J. Magn. Reson 143 (1) (2000) 79–87.
[2] J. Zhou, B. Lal, D.A. Wilson, J. Laterra, P.C. van Zijl, Amide proton transfer (APT) contrast for imaging of brain tumors, Magn. Reson. Med 50 (6) (2003) 1120–1126.
[3] J. Zhou, J.O. Blakeley, J. Hua, M. Kim, J. Laterra, M.G. Pomper, P.C. van Zijl, Practical data acquisition method for human brain tumor amide proton transfer (APT) imaging, Magn. Reson. Med 60 (4) (2008) 842–849.
[4] O. Togao, T. Yoshiura, J. Keupp, A. Hiwatashi, K. Yamashita, K. Kikuchi, Y. Suzuki, S.O. Suzuki, T. Iwaki, N. Hata, M. Mizoguchi, K. Yoshimoto, K. Sagiyama, M. Takahashi, H. Honda, Amide proton transfer imaging of adult diffuse gliomas: correlation with histopathological grades, Neuro. Oncol 16 (3) (2014) 441–448.
[5] O. Togao, A. Hiwatashi, K. Yamashita, K. Kikuchi, J. Keupp, K. Yoshimoto, D. Kuga, M. Yoneyama, S.O. Suzuki, T. Iwaki, M. Takahashi, K. Iihara, H. Honda, Grading diffuse gliomas without intense contrast enhancement by amide proton transfer MR

imaging: comparisons with diffusion- and perfusion-weighted imaging, Eur. Radiol 27 (2) (2017) 578–588.
[6] J. Zhou, E. Tryggestad, Z. Wen, B. Lal, T. Zhou, R. Grossman, S. Wang, K. Yan, D. X. Fu, E. Ford, B. Tyler, J. Blakeley, J. Laterra, P.C. van Zijl, Differentiation between glioma and radiation necrosis using molecular magnetic resonance imaging of endogenous proteins and peptides, Nat. Med 17 (1) (2011) 130–134.
[7] K.J. Park, H.S. Kim, J.E. Park, W.H. Shim, S.J. Kim, S.A. Smith, Added value of amide proton transfer imaging to conventional and perfusion MR imaging for evaluating the treatment response of newly diagnosed glioblastoma, Eur. Radiol 26 (12) (2016) 4390–4403.
[8] J. Zhou, P.C. van Zijl, Defining an Acidosis-Based Ischemic Penumbra from pH-Weighted MRI, Transl. Stroke. Res 3 (1) (2011) 76–83.
[9] D. Momosaka, O. Togao, K. Kikuchi, Y. Kikuchi, Y. Wakisaka, A. Hiwatashi, Correlations of amide proton transfer-weighted MRI of cerebral infarction with clinico-radiological findings, PLoS. One 15 (8) (2020) e0237358.
[10] S.K. Hobbs, G. Shi, R. Homer, G. Harsh, S.W. Atlas, M.D. Bednarski, Magnetic resonance image-guided proteomics of human glioblastoma multiforme, J. Magn. Reson. Imaging 18 (5) (2003) 530–536.
[11] A. Sottoriva, I. Spiteri, S.G. Piccirillo, A. Touloumis, V.P. Collins, J.C. Marioni, C. Curtis, C. Watts, S. Tavare, Intratumor heterogeneity in human glioblastoma reflects cancer evolutionary dynamics, Proc. Natl. Acad. Sci. USA 110 (10) (2013) 4009–4014.
[12] D.J. Aum, D.H. Kim, T.L. Beaumont, E.C. Leuthardt, G.P. Dunn, A.H. Kim, Molecular and cellular heterogeneity: the hallmark of glioblastoma, Neurosurg. Focus 37 (6) (2014) E11.
[13] P.Z. Sun, Y. Murata, J. Lu, X. Wang, E.H. Lo, A.G. Sorensen, Relaxation-compensated fast multislice amide proton transfer (APT) imaging of acute ischemic stroke, Magn. Reson. Med 59 (5) (2008) 1175–1182.
[14] W.T. Dixon, I. Hancu, S.J. Ratnakar, A.D. Sherry, R.E. Lenkinski, D.C. Alsop, A multislice gradient echo pulse sequence for CEST imaging, Magn. Reson. Med 63 (1) (2010) 253–256.
[15] H. Zhu, C.K. Jones, P.C. van Zijl, P.B. Barker, J. Zhou, Fast 3D chemical exchange saturation transfer (CEST) imaging of the human brain, Magn. Reson. Med 64 (3) (2010) 638–644.
[16] E. Sartoretti, T. Sartoretti, C. Binkert, A. Najafi, A. Schwenk, M. Hinnen, L. van Smoorenburg, B. Eichenberger, S. Sartoretti-Schefer, Reduction of procedure times in routine clinical practice with Compressed SENSE magnetic resonance imaging technique, PLoS. One 14 (4) (2019) e0214887.
[17] H. She, J.S. Greer, S. Zhang, B. Li, J. Keupp, A.J. Madhuranthakam, I.E. Dimitrov, R.E. Lenkinski, E. Vinogradov, Accelerating chemical exchange saturation transfer MRI with parallel blind compressed sensing, Magn. Reson. Med 1 (2019) 504–513.
[18] T. Wada, C. Tokunaga, O. Togao, A. Hiwatashi, K. Kikuchi, M. Yoneyama, K. Kobayashi, T. Kato, K. Yoshimoto, K. Ishigami, H. Yabuuchi, Three-dimensional chemical exchange saturation transfer imaging using compressed SENSE for full z-spectrum acquisition, Magn. Reson. Imaging 92 (2022) 58–66.
[19] WHO classification of Tumours Editorial Board. Central nervous system tumours. Lyon (France) : International Agency for Research on Cancer ; 2021 (WHO Classification of tumours series, 5th ed. ; vol.6).
[20] O. Togao, A. Hiwatashi, J. Keupp, K. Yamashita, K. Kikuchi, T. Yoshiura, M. Yoneyama, M.J. Kruiskamp, K. Sagiyama, M. Takahashi, H. Honda, Amide Proton Transfer Imaging of Diffuse Gliomas: Effect of Saturation Pulse Length in Parallel Transmission-Based Technique, PLoS. One 11 (5) (2016) e0155925.
[21] E.A.H. Warnert, T.C. Wood, F. Incekara, G.J. Barker, A.J.P. Vincent, J. Schouten, J. M. Kros, M. van den Bent, M. Smits, J.A.H. Tamames, Mapping tumour heterogeneity with pulsed 3D CEST MRI in non-enhancing glioma at 3 T, MAGMA 35(1) 2922 53-62.
[22] A. Sakata, T. Okada, A. Yamamoto, M. Kanagaki, Y. Fushimi, T. Okada, T. Dodo, Y. Arakawa, B. Schmitt, S. Miyamoto, K. Togashi, Grading glial tumors with amide proton transfer MR imaging: different analytical approaches, J. Neurooncol 122 (2) (2015) 339–348.
[23] M. Doneva, J. Keupp, S. Hey, O. Togao, T. Yoshiura, Comparison of 3D acquisition techniques for amide proton transfer in brain tumor applications, Proc. Int. Soc. Magn. Reson. Med 21 (2013) 4233.
[24] A. Deshmane, M. Zaiss, T. Lindig, K. Herz, M. Schuppert, C. Gandhi, B. Bender, U. Ernemann, K. Scheffler, 3D gradient echo snapshot CEST MRI with low power saturation for human studies at 3T, Magn. Reson. Med 81 (4) (2019) 2412–2423.
[25] J. Zhou, H. Zhu, M. Lim, L. Blair, A. Quinones-Hinojosa, S.A. Messina, C. G. Eberhart, M.G. Pomper, J. Laterra, P.B. Barker, P.C. van Zijl, J.O. Blakeley, Three-dimensional amide proton transfer MR imaging of gliomas: Initial experience and comparison with gadolinium enhancement, J. Magn. Reson. Imaging 38 (5) (2013) 1119–1128.
[26] O. Togao, J. Keupp, A. Hiwatashi, K. Yamashita, K. Kikuchi, M. Yoneyama, H. Honda, Amide proton transfer imaging of brain tumors using a self-corrected 3D fast spin-echo dixon method: Comparison With separate B0 correction, Magn. Reson. Med 77 (6) (2017) 2272–2279.
[27] D. Paech, J. Windschuh, J. Oberhollenzer, C. Dreher, F. Sahm, J.E. Meissner, S. Goerke, P. Schuenke, M. Zaiss, S. Regnery, S. Bickelhaupt, P. Baumer, M. Bendszus, W. Wick, A. Unterberg, P. Bachert, M.E. Ladd, H.P. Schlemmer, A. Radbruch, Assessing the predictability of IDH mutation and MGMT methylation status in glioma patients using relaxation-compensated multi-pool CEST MRI at 7.0 Tesla, Neuro. Oncol 20 (12) (2018) 1661–1671.